Higher Order Tunable Fano Resonances in Multilayer Nanocones

Adnan Daud Khan · Giovanni Miano

Abstract We present a computational study of the plasmonic response of a gold–silica–gold multilayered nanostructure based on truncated nanocones. Symmetry breaking is introduced by rotating the nanostructure and by offsetting the layers. Nanocones with coaxial multilayers show dipole–dipole Fano resonances with resonance frequencies depending on the polarization of the incident light, which can be changed by rotating the nanostructure. By breaking the axial symmetry, plasmonic modes of distinct angular momenta are strongly mixed, which provide a set of unique and higher order tunable Fano resonances. The plasmonic response of the multilayered nanocones is compared to that of multishell nanostructures with the same volume and the former are discovered to render visible high-order dark modes and to provide sharp tunable Fano resonances. In particular, higher order tunable Fano resonances arising in non-coaxial multilayer nanocones can vary the plasmon lines at various spectral regions simultaneously, which makes these nanostructures greatly suitable for plasmon line shaping both in the extinction and near field spectra.

Keywords Nanocones · Plasmon coupling · Higher order hybridized modes · Fano resonance · Symmetry breaking

Introduction

Surface plasmons, which are the combined oscillations of conduction and bound electrons in metallic nanoparticles driven by an external electromagnetic field at optical frequencies, are accountable for the considerable enhancement of the electric field in the vicinity of metallic nanoparticles and for the rich and complex features of the scattered light. The surface plasmon resonances strongly depend on the nanoparticle shape, the nature of metal, and the refractive index of the surrounding media [1]. A number of applications, such as chemical and bimolecular sensing, photothermal cancer therapy, metamaterials, and surface-enhanced Raman spectroscopy [2, 3], are based on surface plasmons. Numerous geometries have been proposed to match the needs of the applications such as nanospheres [4], nanoeggs [5], nanocups [6], rods [7], circular disks [8], rings [9], and ellipsoids [10]. In the recent times, complex nanostructures, like plasmonic nanoshells [5], dimers [11], trimers [4], quadrumer clusters [12], heptamers [13], pentamers [14], and nanoparticle chains [15], have received a huge amount of attention.

The plasmon oscillations of multilayer nanoparticles can be explained in terms of the interaction between the plasmon modes of the single parts of the nanostructure, as they act one by one. For example, the plasmon modes of a metallic nanoshell, composed of a dielectric core and a metallic layer, can be considered as arising from the interaction between the dipolar mode of the metallic sphere $|s\rangle$ and the dipolar mode of the dielectric cavity $|c\rangle$ [16]. The hybridization of the sphere and cavity plasmons created two new plasmon modes, that is, the higher energy-antibonding mode $|+\rangle$ and the lower energy bonding mode $|-\rangle$, corresponding to the antisymmetric and symmetric interactions between the $|s\rangle$ and $|c\rangle$ modes, respectively. A more fine classification consists in distinguishing the plasmon modes of these nanostructures in superradiant and subradiant modes. A superradiant plasmon mode radiates strongly because the dipole modes of the single parts of the multilayer nanostructure are aligned and oscillate in phase, instead a subradiant plasmon mode radiates weakly because the dipolar modes of single parts are aligned oppositely.

A. D. Khan · G. Miano (✉)
Department of Electrical Engineering, University of Naples "Federico II", via Claudio 21,
80125 Naples, Italy
e-mail: miano@unina.it

A. D. Khan
e-mail: adnandaud.khan@unina.it

Multilayer nanostructures display Fano-like resonances in their optical spectra, which appear from the coupling and interference of bright and dark plasmon modes. The Fano-like shape is quite different from the symmetric Lorentzian resonance and it is analogous to the electromagnetic-induced transparency [17]. The interactions between hybridized bright modes and dark modes can be increased through the symmetry breaking, due to which bright dipolar modes both constructively and destructively interfere with the higher order dark multipolar modes, which results in additional Fano resonances [8, 18]. The symmetry breaking conception has been initiated in a variety of plasmonic nanostructures to attain higher order Fano resonances. In plane ring/disk nanocavities, offsetting the central disk results in a coherent interaction between the bright dipolar mode of the disk and dark multipolar mode of the ring, which engenders dipole–quadrupole Fano resonances. In nanoparticle aggregates, modifying the size of one of the nanoparticles or the gap between the nanoparticles results in a coupling between bright and dark modes of the structure. Depositing a nanoparticle on a dielectric substrate can also initiate a coupling between dark and bright plasmon modes. Removing a wedge from a metallic nanodisk results in the interaction between a hybridized dipolar plasmon mode of the disk and a narrow quadrupole mode of the wedge-shaped slice, which exhibit a Fano resonance in the optical spectrum. In three-dimensional multilayered nanoshells, displacing the central metallic core can initiate a coupling between dark quadrupolar modes and bright dipolar modes due to which higher order Fano resonances can be perceived in the optical spectrum. All the above-mentioned nanostructures have been recently successfully fabricated and theoretically analyzed using different analytical and numerical techniques [8, 18–21].

In this paper, we investigated the plasmon coupling in multilayer nanostructures based on silica and truncated gold nanocones, which can be fabricated by methods described in [18, 22]. The unique feature of multilayered conical nanostructures is that a symmetry breaking in the coupling mechanism with the incident electromagnetic field can be simply obtained by rotating them. This cannot be accomplished in nanostructures with spherical symmetries. We started our discussion from a single gold nanocone and moved towards coaxial multilayered nanostructures. Fano resonances are achieved at different frequencies by rotating the nanostructure axis with respect to the incident polarization. Furthermore, the axial symmetry has been broken in two manners. First by offsetting the inner gold cone with respect to the outer shell to make a non-coaxial multilayer nanostructure and then by offsetting both the inner gold cone and middle silica cone to make a multilayered nanoegg cone, which provide unique higher order tunable Fano resonances. The extinction spectra of all the nanostructures are proved to be strongly dependent on the angle and polarization of the incident light. Eventually,

the optical response of the multilayered nanocones is compared to the concentric and nonconcentric multilayered nanospheres and the former nanostructures are discovered to provide higher order dark modes and sharp tunable Fano resonances than the latter nanostructures.

We studied the extinction spectra, the distribution of the induced surface (free and bond) charges, and the near field enhancement of silica–gold nanostructures with truncated conical shape. The optical properties of the proposed nanostructures were not very sensitive to the precise value of the semi-angle α of the conical shape, thus we chose $\alpha=27°$. The near and far field optical responses were computed by COMSOL Multiphysics software with the RF module. Johnson and Christy data have been utilized for the dielectric constant of the gold [23]. The embedding medium was considered air for all the considered cases.

The incident light was a time harmonic linearly polarized plane wave. We used a Cartesian reference system (x, y, z) with the x-axis parallel to the electric field of the incident wave and the z-axis parallel to its propagation direction. We analyzed the optical properties of the nanoparticles by rotating its axis around the y-axis of an angle θ, from $\theta=0°$ to $90°$ (Fig. 1). For $\theta=0°$, the incident light propagates along the nanostructure axis and its electric field is directed transversally, instead for $\theta=90°$, the incident light propagates transversally to the nanostructure and its electric field is directed longitudinally.

Optical Properties of a Multilayered Nanocone

In order to better understand the optical properties of a multilayer gold–silica–gold nanocone, it is appropriate to first study a gold nanocone and then a silica–gold conical nanoshell. The optical response of the multilayer nanocone is analyzed by using the plasmon hybridization theory [16].

Gold Nanocone

We consider the truncated gold nanocone (NC) shown in Fig. 2a. Its radius R_1 and its height H_1 are 85 and 95 nm,
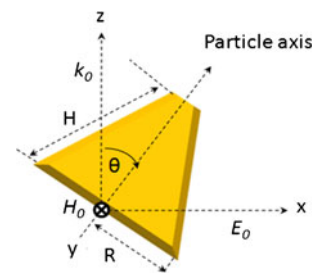
Fig. 1 Sketch of the nanostructure. The incident field is linearly polarized along the x-direction and propagates along the z-direction. The nanoparticle axis is rotated around the y-axis of an angle θ from $0°$ to $90°$

respectively. The extinction spectrum is slightly affected by rotating its axis around the y-axis, as shown in Fig. 2b. The resonance peak at $\theta=0°$ (blue line) is relevant to the transverse dipolar mode as it is corroborated by the charge distribution on the gold surface at 605 nm shown in the inset of Fig. 2b. By increasing θ, the peak amplitude of the transverse dipolar mode weakens, shifts towards the blue, and an axial dipolar mode appears. At $\theta=90°$ (purple line), the dipolar mode is purely axial, as it is confirmed by the surface charge distribution at 556 nm shown in the insets of Fig. 2b. These extinction spectra are typical of gold nanoparticles with cylindrical symmetries.

Silica–Gold Conical Nanoshell

We consider now a conical nanoshell (CNS) composed of a conical silica core, with a relative dielectric constant of 2.04, and a coaxial gold conical shell surrounding the silica cone (Fig. 3a). The dimensions are $R_1=85$ nm, $H_1=95$ nm/$R_2=60$ nm, and $H_2=70$ nm. This nanostructure is obtained by replacing the inner part of the truncated gold nanocone with a truncated silica cone.

We first discuss the optical properties of the CNS for $\theta=0°$. They can be understood by using the plasmon hybridization theory [16]. The plasmon oscillations of the CNS arise from the interaction of the plasmon oscillations supported by the solid gold nanocone and the silica cavity in a gold environment. The interaction occurs between the transverse dipolar mode of the gold nanocone and that of the silica cavity, which splits the transverse dipolar mode into the higher energy antibonding mode $|\omega_+\rangle$ and the lower energy bonding mode $|\omega_-\rangle$. The antibonding mode arises from the antisymmetric coupling between the cone and cavity dipolar modes, which is characterized by a small electric dipole moment. For this reason, the antibonding mode does not appear in the extinction spectrum. Instead, the bonding mode, which arises from the symmetric coupling between the cone and cavity dipolar modes, contributes significantly to the scattered field.

The extinction spectrum of the CNS is highly influenced by the rotation of its axis around the y-axis, as shown in Fig. 3b. For inclined incident wave ($\theta\neq0°$), both the transverse and the longitudinal bonding modes are excited. At $\theta=0°$ (blue line), the hybridization phenomenon of the primitive dipolar modes is stronger than at $\theta=90°$ (purple line). The charge distributions on the outer surface of the gold shell and at the gold–silica interface, relevant to the transverse (at 694 nm, $\theta=0°$) and axial (at 581 nm, $\theta=90°$) bonding modes, are shown in the inset of Fig. 3b. They are the typical distributions of the dipolar charge configurations.

Multilayered Nanocone

We here consider a truncated multilayered nanocone (MNC) composed of an inner gold cone, a middle silica layer, and an outer gold shell, as shown in Fig. 4a (side view) and b (top view). This nanostructure is obtained by replacing the inner part of a silica–gold conical nanoshell with a coaxial gold nanocone. The addition of the inner gold nanocone will provide an extra degree of tunability as in spherical multilayer nanoshells [18, 24–26]. The dimensions of the nanostructure are $R_1=85$ nm, $H_1=95$ nm/$R_2=60$ nm, $H_2=70$ nm/$R_3=40$ nm, and $H_3=50$ nm.
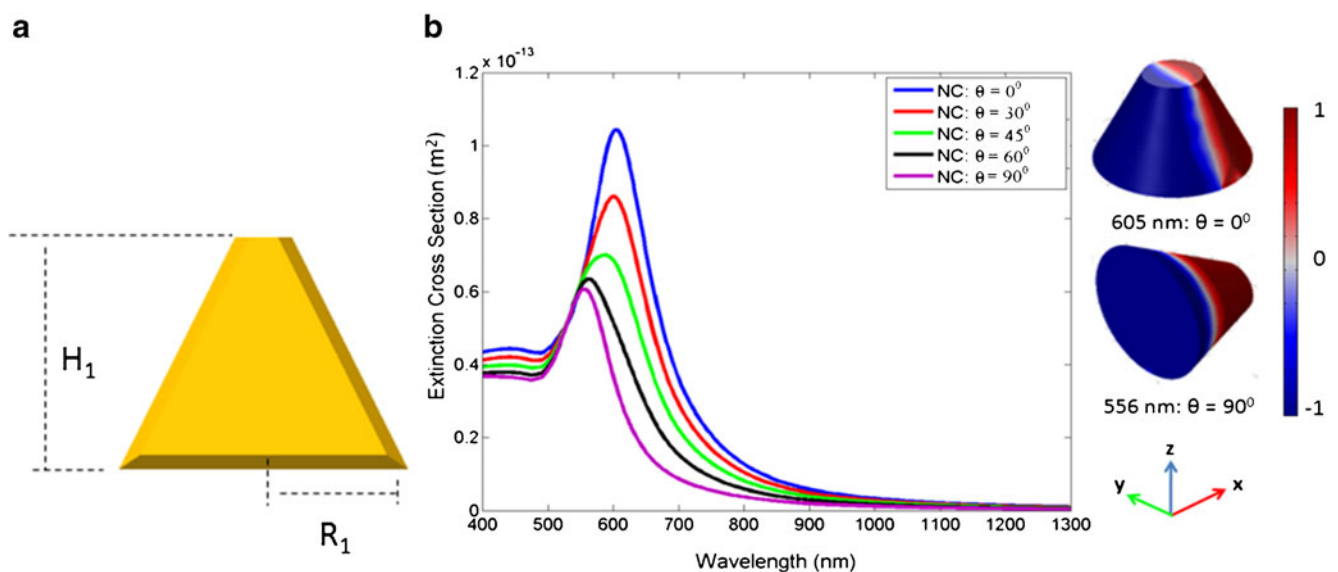
Fig. 2 **a** Gold nanocone with $R_1=85$ nm and $H_1=95$ nm. **b** Extinction spectra at different angles θ. *Inset* shows the surface charge distributions relevant to the transverse (at 605 nm) and axial (at 556 nm) dipolar modes
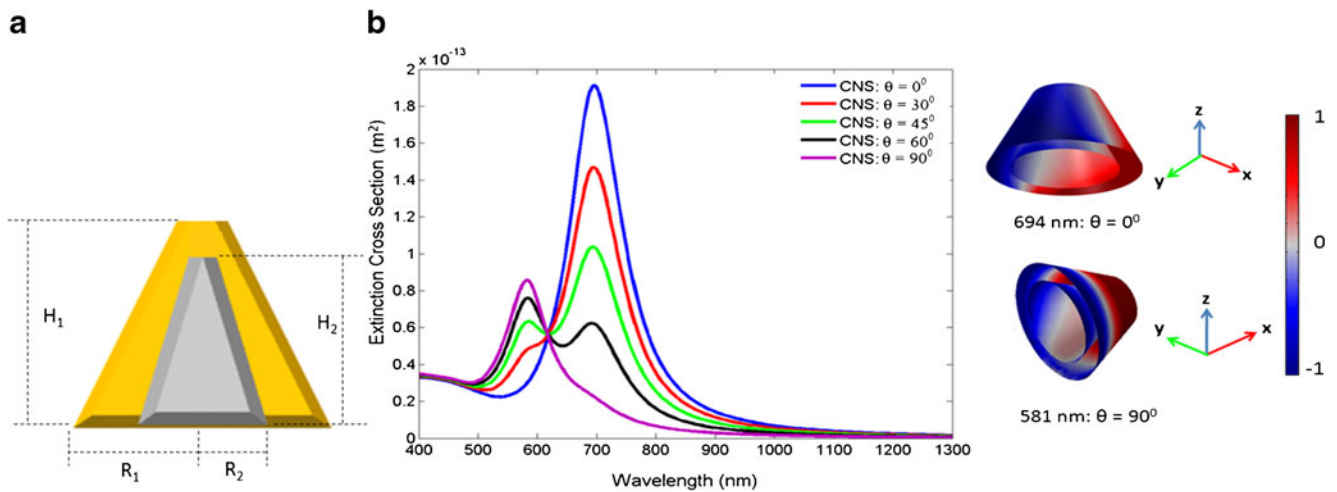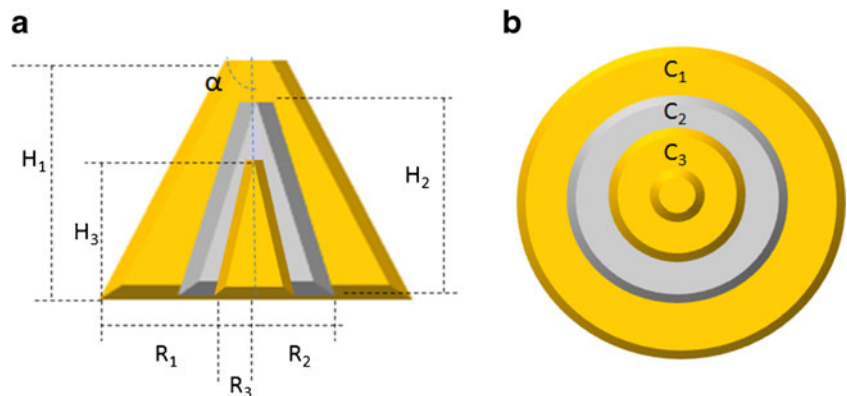
Fig. 3 a Silica–gold conical nanoshell with R_1=85 nm, H_1=95 nm/R_2=60 nm, and H_2=70 nm. b Extinction spectra at different values of the angle θ. *Inset* shows the surface charge distributions relevant to the transverse (at 694 nm) and axial (at 581 nm) dipolar modes

To interpret the optical response of the MNC, we again employ the plasmon hybridization theory, but at this time, we apply it to the inner gold nanocone and the outer silica–gold conical nanoshells [26–28]. Figure 5 shows the extinction spectra of the MNC for θ=0° (transverse polarization of the incident field), including the extinction spectra of the inner gold nanocone and the outer silica–gold conical nanoshell. The extinction spectrum of the inner gold cone is very similar to that shown in Fig. 2b for θ=0°, apart a blueshift of some tens of nanometers. The hybridization will emerge between the dipole mode $|\omega_b\rangle$ of the inner gold cone, which has a resonance at roughly 560 nm, and the dipole-bonding mode $|\omega_-\rangle$ of the outer conical nanoshell, which has a resonance at roughly 694 nm. The mode $|\omega_b\rangle$ interacts with the mode $|\omega_-\rangle$ and two different resonant peaks in the extinction spectrum as in spherical multilayer nanoshells arise [18, 27, 29]. The high-energy peak near 600 nm is relevant to a broad antibonding plasmon mode $|\omega_-^+\rangle_{(1)}$ that arises from the symmetric coupling between the modes $|\omega_b\rangle$ and $|\omega_-\rangle$. Instead, the lower energy peak near 811 nm is relevant to a narrow bonding plasmon mode $|\omega_-^-\rangle_{(1)}$ that

originates from the antisymmetric coupling between the modes $|\omega_b\rangle$ and $|\omega_-\rangle$. The surface charge distributions in correspondence of the two peaks and the dip in the extinction spectrum are shown in the insets of Fig. 5. They are of dipolar type. The charges are induced on three surfaces: the air–gold shell interface S_1 (outer surface), the gold shell–silica shell interface S_2 (intermediate interface), and the silica shell–gold cone interface S_3 (inner interface). At 600 nm, the dipole moment P_3 of the charge distribution on S_3 and the overall dipole moment P_{1-2} of the charge distributions on S_1 and S_2 oscillate in phase (superradiant dipolar mode), whereas at 811 nm, they oscillate out of phase (subradiant dipolar mode). At 719 nm, where a deep dip appears in the extinction spectrum, the surface charge distribution is very similar to that corresponding to the peak at 600 nm, but the intensity of P_{1-2} is much weaker.

The coexistence of the broad dipolar mode $|\omega_-^+\rangle_{(1)}$ and the narrow dipolar mode $|\omega_-^-\rangle_{(1)}$, which are resonant over the same range of wavelengths, can result in a coupling between them and, therefore, they can produce a dipole–dipole Fano resonance. Figure 6 shows the extinction

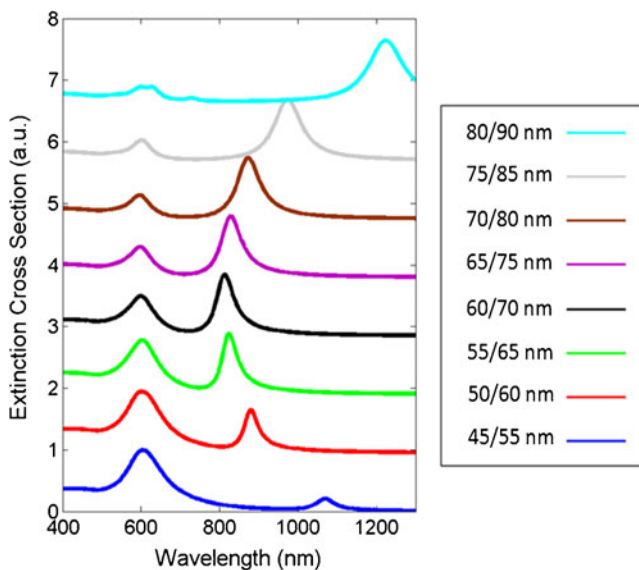Fig. 4 Side (a) and top (b) views of the gold–silica–gold multilayer nanocone
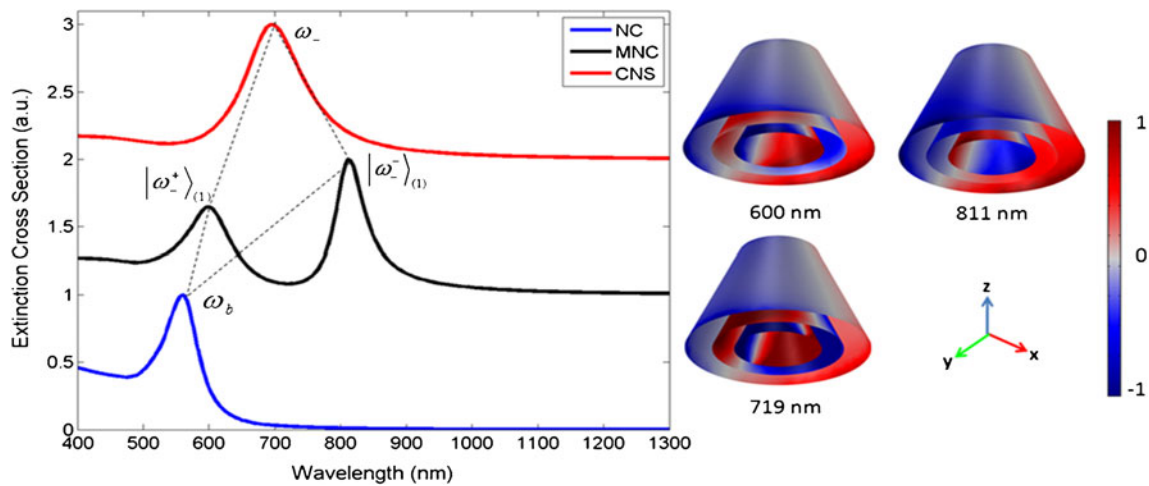
Fig. 5 Plasmon mode hybridization in the multilayer nanocone with $R_1=85$ nm, $H_1=95$ nm/$R_2=60$ nm, $H_2=70$ nm/$R_3=40$ nm, and $H_3=50$ nm. *Bottom and top panels* show, respectively, the extinction cross sections of the gold nanocone and the silica–gold conical nanoshells, while *middle panel* shows the extinction cross section of the combined structure. *Inset* shows the charge distributions corresponding to the peaks at 600 and 811 nm, as well as to the dip at 719 nm
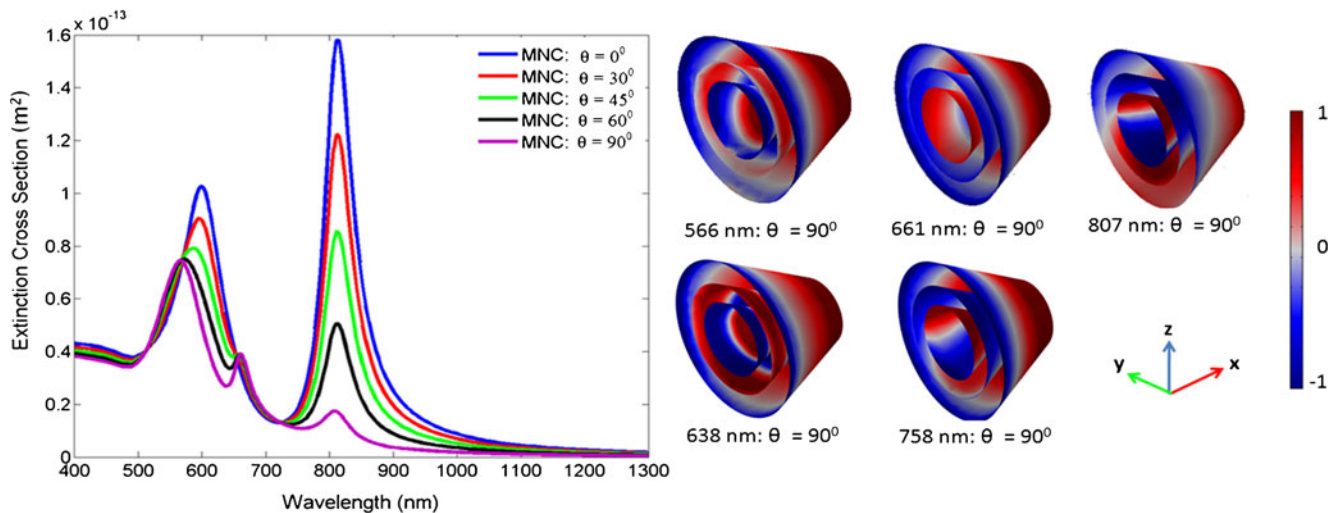
spectra of the MNC with different values of the core–shell aspect ratio. Here (H_1,R_1) and (H_3,R_3) are fixed at (85 nm, 95 nm) and (40 nm, 50 nm), respectively, instead, the values of H_2 and R_2 are increased in such a way to leave unchanged the semi-angle α. The increasing of R_2 leads to the increase of the separation between the inner gold core and outer gold shell and the decrease of the outer gold shell thickness. The intensity of the $|\omega_-^+\rangle_{(1)}$ dipole peak decreases significantly as the radius of the silica R_2 increases, while its position is practically unaffected. When the R_2 value is small, with the increase of R_2, the $|\omega_-^-\rangle_{(1)}$ dipole peak shows a blueshift,

Fig. 6 Extinction spectra of the multilayer nanocone for different values of (H_2,R_2) with $R_1=85$ nm, $H_1=95$ nm/$R_3=40$ nm, and $H_3=50$ nm

which will enhance the coupling between the $|\omega_-^+\rangle_{(1)}$ and $|\omega_-^-\rangle_{(1)}$ modes. They interact through the near field and a sharp dipole–dipole Fano resonance turns up in the extinction spectrum, with a Fano dip around 719 nm for $R_2=60$ nm [15, 27, 28]. When the R_2 value is large enough, by increasing further the R_2 value, the $|\omega_-^-\rangle_{(1)}$ dipole peak shows a redshift and the coupling becomes weak. When the distance is sufficiently high, the $|\omega_-^-\rangle_{(1)}$ dipole mode does not couple with the $|\omega_-^+\rangle_{(1)}$ dipole mode and, hence, the dipole–dipole Fano resonance vanishes. Thus, by controlling the dimensions of the MNC, we can have a pronounced Fano resonance for the coaxial case as well. Higher order dark modes do not appear for $\theta=0°$.

Figure 7 shows the extinction spectra obtained by rotating the MNC axis around the *y*-axis for different values of θ and the surface charge distributions for $\theta=90°$ in correspondence of the peaks and dips in the extinction spectrum. The peak at 807 nm weakens but does not disappear at $\theta=90°$ like in the simple CNS. The phase variation of the incident wave produces a strong hybridization between the axial and transverse dipolar modes. The surface charge distribution corresponding to the weakly dip at 758 nm shows a similar hybridization even if in a more weak form. A new peak at 661 nm emerges in the spectrum, which clearly shows the appearance of a further axial dipolar mode, beside that relevant to the peak at 566 nm. The dipolar mode at 566 nm is a superradiant longitudinal mode while that at 661 nm is a subradiant one. The interaction between them give arises to a dipole–dipole Fano dip at 638 nm. The charge distribution relevant to this dip is very similar to that of the superradiant mode as for $\theta=0°$. The considered MNC shows two dipole–dipole Fano resonances,

Fig. 7 Extinction spectra of the multilayer nanocone with R_1=85 nm, H_1=95 nm/R_2=60 nm, H_2=70 nm/R_3=40 nm, and H_3=50 nm for different values of the rotation angle θ. *Inset* shows the surface charge distributions at five values of the wavelength for θ=90°

one at 638 nm and the other at 758 nm, which can be switched on and off by rotating the nanostructure or by changing the polarization of the incident field. To our knowledge, this hybridization has never been seen in a symmetric multilayered plasmonic nanostructures reported before.
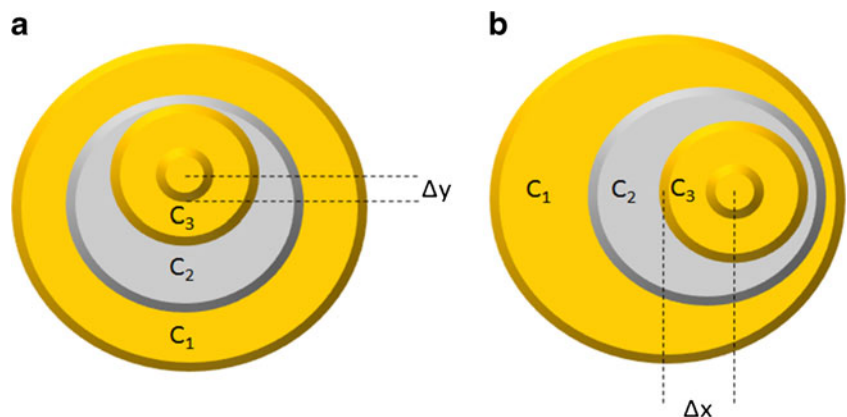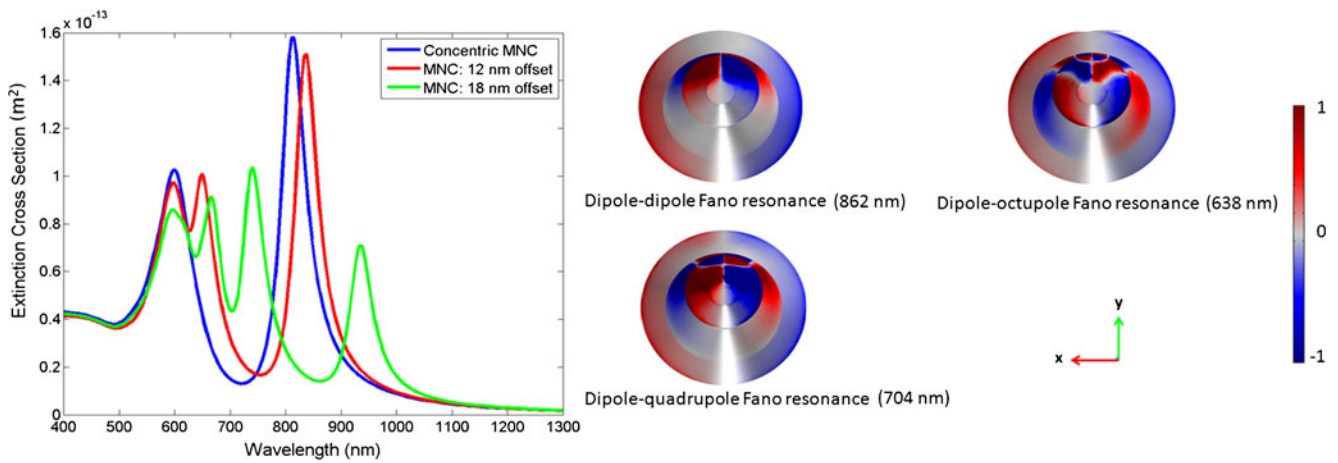
Non-Coaxial MNC

We consider now a MNC in which the inner gold cone is offset with respect to the shell nanostructure. We named this nanostructure a non-coaxial MNC (NC-MNC). In it, modes with different orders and having distinctive angular momenta will mix due to the symmetry breaking introduced by the offset [18, 26, 28, 30]. We analyze the consequences of this symmetry breaking by distinguishing between the case in which the inner gold cone is offset along the direction of the incident E-field or it is offset along the orthogonal direction (Fig. 8).

In Fig. 9, we show the extinction spectra of a NC-MNC in which the inner gold cone is offset orthogonally to the

incident E-field, for two values of the offset and θ=0°. They are compared with the extinction spectrum of the corresponding coaxial MNC (blue curve). For a 12-nm core offset (red curve), a dark quadrupolar peak $\left|\omega_-^-\right\rangle_{(2)}$ with added dipolar components emerges in the spectrum, which couples to the $\left|\omega_-^+\right\rangle_{(1)}$ mode and engenders a dipole–quadrupole Fano resonance with a minimum near 625 nm. By offsetting the gold cone slightly more (18 nm), besides the redshift of the Fano resonances, a dark octupolar peak $\left|\omega_-^-\right\rangle_{(3)}$ emerges, which couples to the $\left|\omega_-^+\right\rangle_{(1)}$ mode and churn out a dipole–octupole Fano resonance with a dip near 646 nm (green curve). We also note that the modes $\left|\omega_-^-\right\rangle_{(1)}$ and $\left|\omega_-^-\right\rangle_{(2)}$ are redshifted and their peak amplitudes reduce with the core offset, whereas the $\left|\omega_-^+\right\rangle_{(1)}$ mode is faintly blueshifted, because it is a high-energy mode and has an extremely feeble interaction with the gold cone dipolar mode [25]. The surface charge distributions corresponding to the dipole, quadrupole, and octupole Fano resonances

Fig. 8 Geometry of a NC-MNC with core offset Δy, orthogonally to the incident E-field (**a**). Geometry of a MNEC with two component offset Δx, parallel to the incident E-field (**b**)

Fig. 9 Extinction spectra of a MNC (R_1=85 nm, H_1=95 nm/R_2= 60 nm, H_2=70 nm/R_3=40 nm, H_3=50 nm) with core offset orthogonally to the incident E-field. *Blue line* corresponds to the coaxial MNC, while the *red and green lines* correspond to NC-MNC with 12 and 18 nm core offsets, respectively. The *inset* shows the surface charge distributions associated with the dipole–dipole, dipole–quadrupole, and dipole–octupole Fano resonances for the 18-nm core offset

with added dipolar components are shown in the inset of Fig. 9 for the 18-nm core offset. For the dipole–quadrupole Fano resonance, the charges on the shell exhibit a dipolar arrangement, while that on the surface of the inner core exhibit a quadrupolar arrangement, which evidently reveals the mixing of dipole and quadrupole modes. Likewise, for the dipole–octupole Fano resonance, the surface charge distribution exhibits the mixing of dipole and octupole modes.

Figure 10 shows the extinction spectra of the NC-MNC with 18 nm core offset obtained by rotating the nanoparticle axis around the y-axis. At θ=90°, the higher order modes weaken and start to disappear in the spectrum but still the $\left|\omega_-^-\right\rangle_{(1)}$ and $\left|\omega_-^-\right\rangle_{(2)}$ modes are present somewhat. The peak positions relevant to the $\left|\omega_-^-\right\rangle_{(1)}$ and $\left|\omega_-^-\right\rangle_{(2)}$ modes are almost independent of the angle θ. A slightly new peak

appears at the low-energy level near 1,034 nm, which also represents a bonding $\left|\omega_-^-\right\rangle_{(1)}$ mode. At θ=90°, we obtained almost no Fano resonance in the spectrum.

Figure 11 shows the extinction spectra of a NC-MNC in which the inner gold cone is offset parallel to the direction of the incident E-field, for the two values of the offset (12 and 18 nm), together with the charge distributions for the 18-nm core offset. Here, we obtain one more peak in the extinction spectra for both the offset values. For 12 nm core offset (red line), we obtained four extinction peaks in the spectrum. The peak near 698 nm also represents a subradiant dipole mode while the peak near 647 nm represents a quadrupole mode. For 18 nm core offset, both the dipole and quadrupole peaks redshift and a new quadrupole peak is observed near 655 nm as shown by the surface charge distributions. The peak near 1,034 nm is relevant to the $\left|\omega_-^-\right\rangle_{(1)}$ plasmon mode. The peak around 867 nm exhibits a ring-shaped dipolar pattern on the inner cone and a half ring shape on the outer cone. It is also relevant to a $\left|\omega_-^-\right\rangle_{(1)}$ plasmon mode. The peaks near 718 and 655 nm are relevant to the $\left|\omega_-^-\right\rangle_{(2)}$ plasmon mode. Thus, by offsetting the gold cone parallel to the incident E-field, we can have twin dipole and quadrupole Fano resonances at different frequencies both in the visible and near infrared region. Figure 12 shows the extinction spectra of the NC-MNC with 18 nm core offset parallel to the incident E-field, obtained by rotating the nanoparticle axis around the y-axis. Again at θ=90°, the higher order modes weaken and start to disappear in the spectrum but still the $\left|\omega_-^-\right\rangle_{(1)}$ modes are present somewhat. The peak position of $\left|\omega_-^-\right\rangle_{(1)}$ modes is almost independent of the angle θ. Again at θ=90°, we obtained almost no Fano resonance in the spectrum.
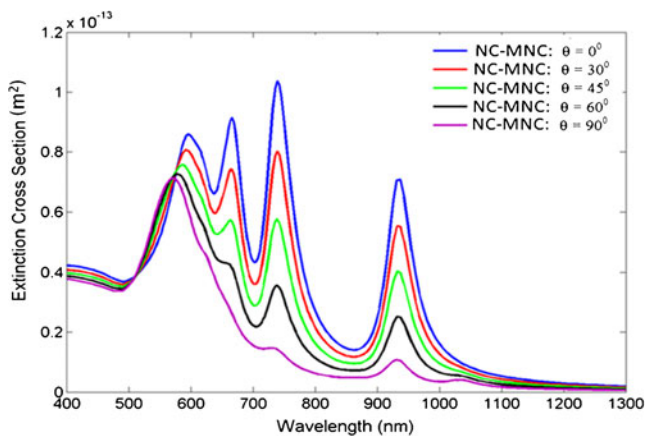
Fig. 10 Extinction spectra of the NC-MNC (R_1=85 nm, H_1=95 nm/ R_2=60 nm, H_2=70 nm/R_3=40 nm, H_3=50 nm) with core offset of 18 nm orthogonally to the incident E-field, for different values of the rotation angle of the nanostructure axis around the y-axis
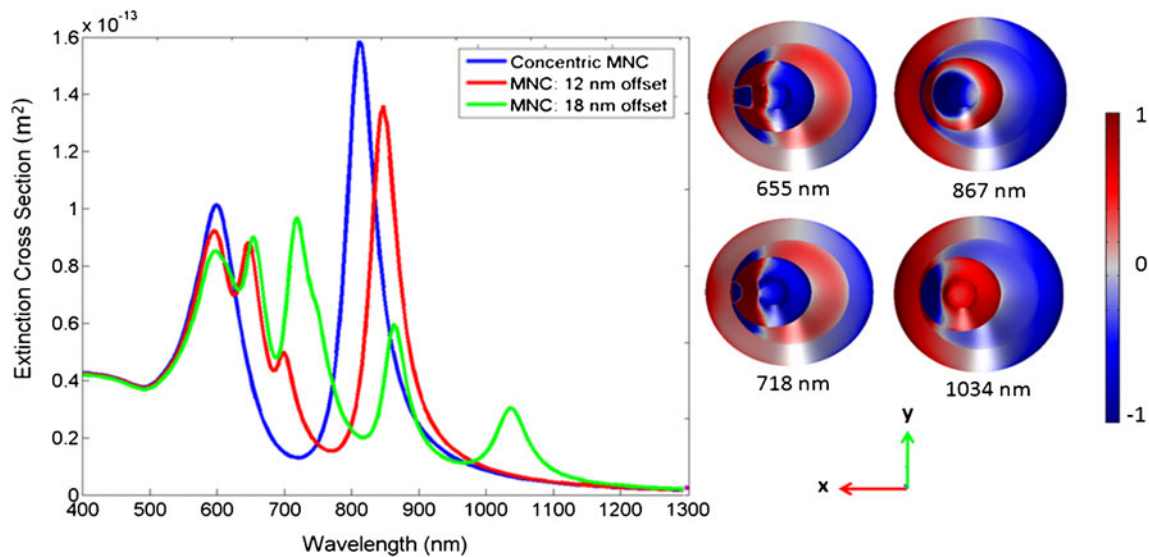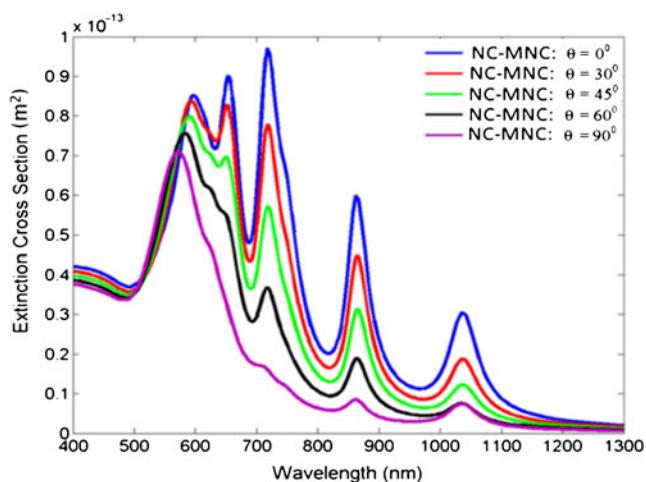
Fig. 11 Extinction spectra of a MNC (R_1=85 nm, H_1=95 nm/R_2= 60 nm, H_2=70 nm/R_3=40 nm, H_3=50 nm) with core offset parallel to the incident E-field. *Blue line* corresponds to the coaxial MNC, while the *red and green lines* correspond to NC-MNC with 12 and 18 nm core offsets. *Inset* shows surface charge distributions of the plasmon modes relevant to peaks in the extinction spectrum for the 18-nm core offset

Multicomponent Offset in MNC (MNEC)

We finally break the symmetry of the MNC with two offsets, i.e., both the inner gold cone and silica cone are moved with respect to the outer gold cone. In this way, we obtain a shape that when seen from the top, it looks like a multilayered nanoegg. We named this nanostructure a multilayered nano-egg cone (MNEC). Figure 13a shows the extinction spectrum of the MNEC in which the silica shell has been moved 18 nm and the inner gold cone has been moved 36 nm in the
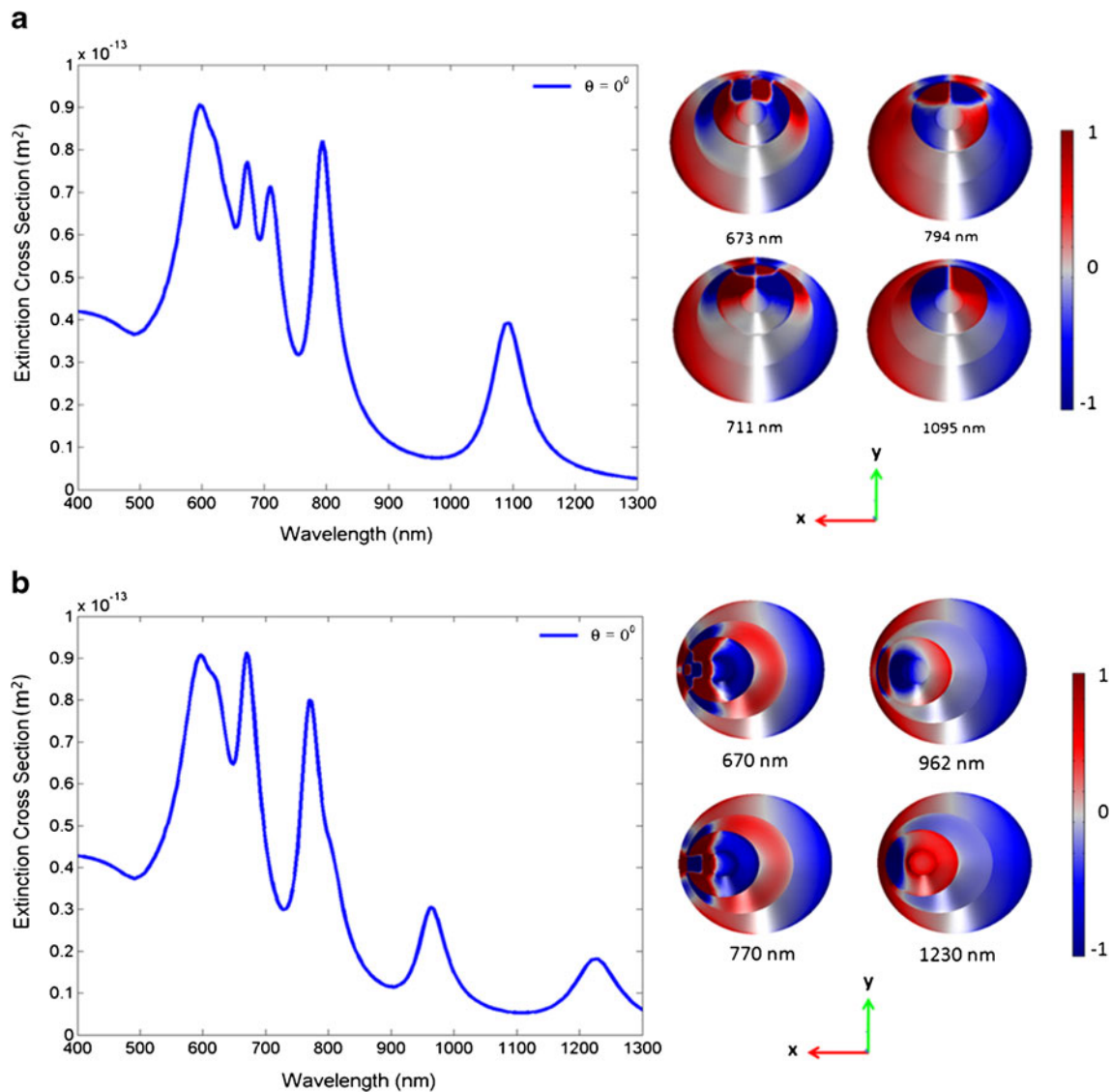

Fig. 12 Extinction spectra of the NC-MNC (R_1=85 nm, H_1=95 nm/ R_2=60 nm, H_2=70 nm/R_3=40 nm, H_3=50 nm) with core offset of parallel to the incident E-field, for different values of the rotation angle of the nanostructure axis around the *y*-axis

y-direction (orthogonal to the incident E-field) for θ=0°. Figure 13b shows the same configuration but with the offset in the *x*-direction (parallel to the incident E-field). Five peaks emerge in the extinction spectrum. Observing the surface charge distribution corresponding to each peak of the extinction spectrum of Fig. 13a, we perceive that the resonant peak near 1,095 nm is a subradiant dipole mode. The resonant peak near 794 nm is a quadrupole–quadrupole mode, as the surface charges on both the shell and inner cone exhibits a quadrupole pattern, which apparently reveals the mixing. Since the symmetry of the CNS is also broken in this structure, so higher order modes of the outer cone will also become visible. The peak around 711 nm patently exhibits the mixed octupole–quadrupole character of the octupole–quadrupole mode and the peak around 673 nm is the combination of octupole modes. Figure 13b shows the extinction spectrum of the MNEC when the multicomponent offset is parallel to the E-field. The peaks near 962 and 1,230 nm represent dipole–dipole modes, while the peak near 770 nm displays an octupole–quadrupole pattern and the peak around 670 nm is a mixture of octupole modes. Therefore, geometries with multicomponent offset have five distinct peaks and pronounced Fano resonances in the extinction spectrum.

Comparison with Multilayered Spherical Nanostructure

We conclusively compare the near and far field optical properties of the gold–silica–gold MNC and NC-MNC with

Fig. 13 Extinction spectra of a MNEC (R_1=85 nm, H_1=95 nm/R_2=60 nm, H_2=70 nm/R_3=40 nm, H_3=50 nm) with multicomponent offsets orthogonal (**a**) and parallel (**b**) to the incident E-field, for θ=0°. *Inset* shows the surface charge distributions (*top view*) relevant to the last four peaks

a concentric multilayered nanosphere (MNS) and a non-concentric MNS (NC-MNS), by taking all the nanostructures with the same volume.

By considering the far field properties first, we observed a sharp dipole–dipole Fano resonance in the extinction spectrum of the MNC compared to those observed in the MNS, as shown in Fig. 14a. Figure 14b shows the extinction spectra of the NC-MNC and the NC-MNS with a 45 % core offset orthogonally to the direction of the incident E-field. As a consequence of the symmetry breaking, additional Fano resonances arise in the spectrum. The modulation depths of the dipole, quadrupole, and octupole Fano resonances in the case of the NC-MNC are found to be larger and sharper compared to those

observed in the NC-MNS nanostructure. Figure 14c shows the extinction spectra of both the structures with a 45 % core offset parallel to the direction of the incident E-field. We obtained five peaks in case of NC-MNC, which proves its strength in the generation of higher order Fano resonances compared to NC-MNS. The dominant scattering and absorption cross sections of both the MNC and NC-MNC may be considered as excellent candidates for the bio-imaging and photothermal treatment applications [3].

We eventually compare the Fano resonances in the near field optical properties of the MNC and the NC-MNC with those observed in the MNS and the NC-MNS nanostructures. Figure 15a shows the maximum
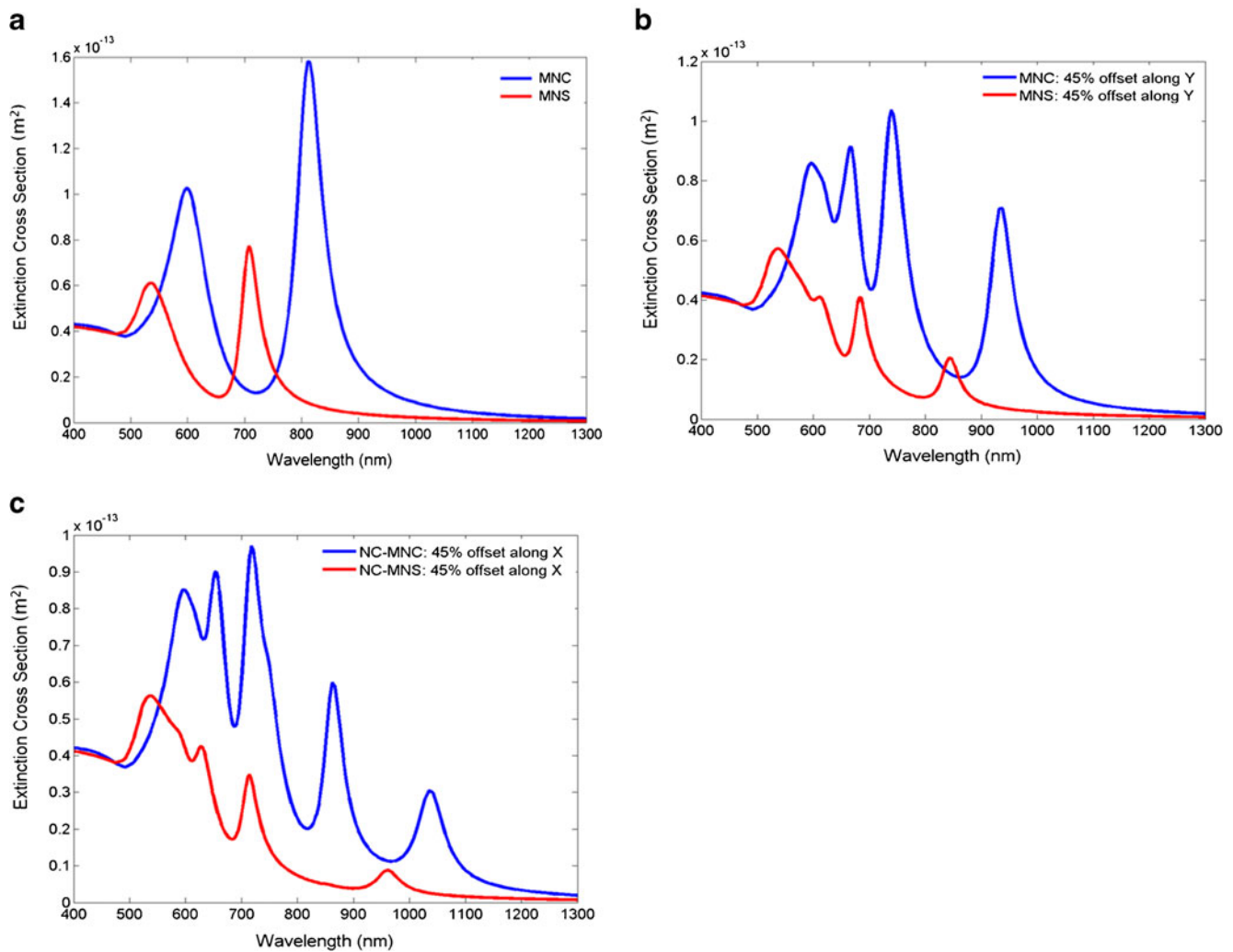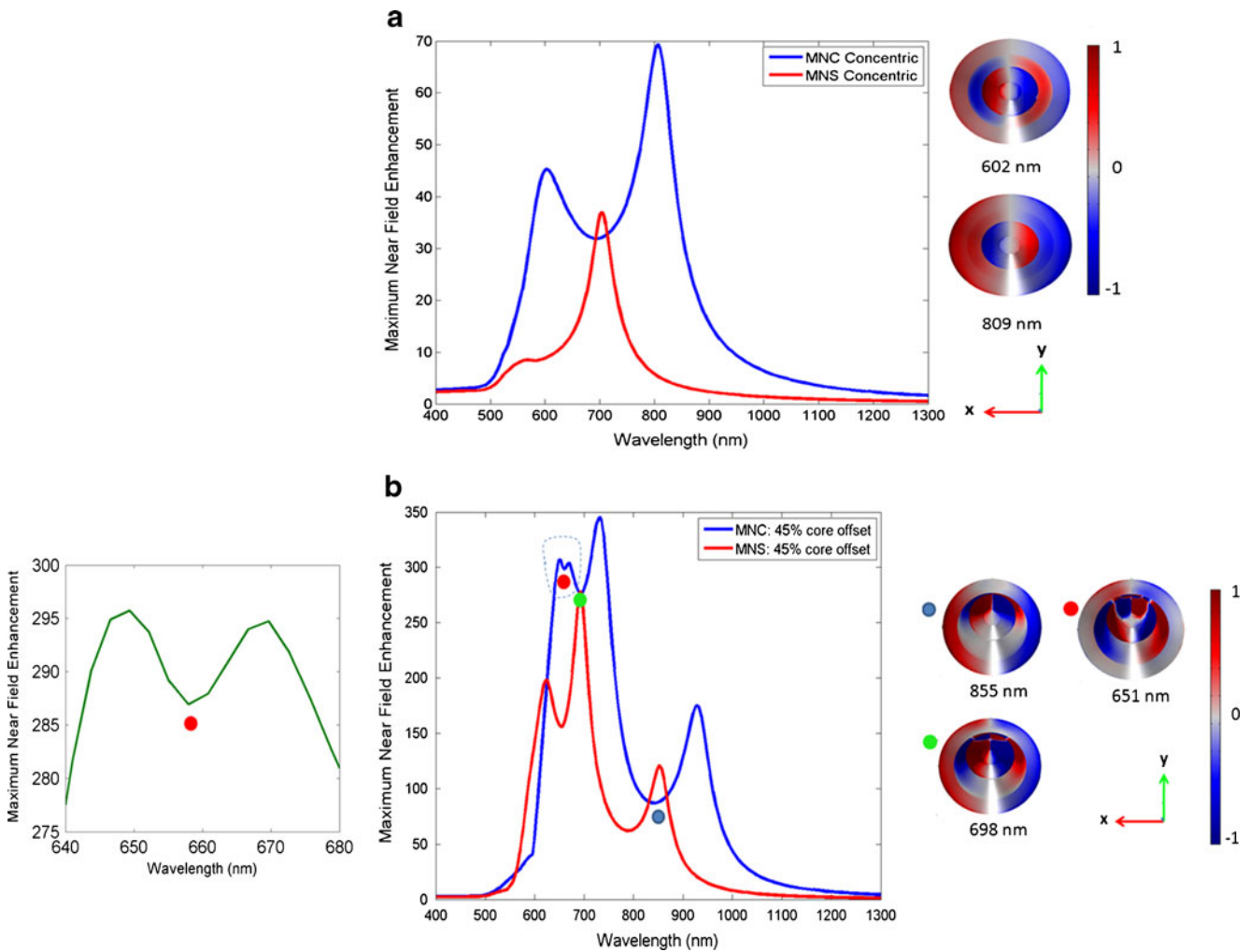
Fig. 14 Extinction cross section. **a** MNC and MNS nanostructures. **b** NC-MNC and NC-MNS with 45 % core offset orthogonally to the incident E-field. **c** NC-MNC and NC-MNS with 45 % core offset parallel to the incident E-field

near field enhancement (MNFE) as a function of wavelength of both the MNC and MNS nanostructures. It is seen that the peaks of near field enhancement for both the MNC and MNS nanostructures emerge almost at the same wavelengths as in the extinction spectra. The MNFE value of the MNC $\left|\omega_-^-\right\rangle_{(1)}$ mode is around 70, which is quite high than the MNS $\left|\omega_-^-\right\rangle_{(1)}$ mode. Figure 15b shows the MNFE of both the NC-MNC and NC-MNS for a 45 % core offset orthogonally to the direction of E-field. It appears that the NC-MNC can provide the excellent enhancement values at various regions in the spectrum compared to NC-MNS nanostructure, which is an important attribute of surface-enhanced Raman spectroscopy (SERS). The surface charge distributions corresponding to each Fano dip are shown in the inset. On the other hand, for the NC-MNS, the octupole mode is missing in the MNFE spectra. From the MNFE spectra, it becomes clear that the energy stored in the

dark hybridized modes is larger than those stored in the bright modes due to the weak radiation losses [31]. Thus, based on the above findings, we concluded that MNC and NC-MNC nanostructures exhibit sharp tunable Fano resonances with large modulation depths both in the near and far field optical properties compared to MNS and NC-MNS nanostructures, which would be useful for multi-wavelength SERS and biosensing.

Conclusion

We have investigated the generation of higher order Fano resonances in a multilayered gold–silica–gold nanostructure with conical shape illuminated by a linearly polarized light. For a coaxial multilayered nanostructure, a sharp dipole–dipole Fano resonance is obtained by varying the relative

Fig. 15 a Maximum near field enhancement of MNC and MNS nanostructures. *Inset* shows surface charge distributions (*top view*) corresponding to each peak in the MNC. **b** NC-MNC and NC-MNS with 45 % core offset orthogonally to the incident E-field. The displayed small window corresponds to the dashed box, which shows the octupole Fano resonance. *Inset* shows surface charge distributions (*top view*) corresponding to each Fano dip (*dot*) in NC-MNC

dimensions of the layers, whose resonance frequencies can be changed by rotating the nanostructure. Two types of breaking of the axial symmetry have been introduced in the multilayered nanostructure: first by offsetting the inner core with respect to the outer shell to make a non-coaxial multilayered nanostructure and then by offsetting simultaneously the inner gold cone and the middle silica cone. In the first case, the coupling between the superradiant dipolar and subradiant higher multipolar modes results in additional Fano resonances in the optical spectrum compared to the coaxial multilayered nanostructure. If the offset is parallel to the incident E-field, we have twin dipole and quadrupole Fano resonances at different frequencies both in the visible and near infrared region. Multicomponent offsetting in MNEC nanostructures renders visible highorder dark modes and provides sharp tunable Fano resonances. Finally, we relate the near and far field optical properties of MNC and NC-MNC with MNS and NC-MNS nanostructures and observed strong tunable higher order Fano resonances in case of MNC and NC-MNC. The maximum near field enhancement is also found to be greater in various regions in both the MNC and NC-MNC nanostructures, which is an essential feature of SERS. To conclude, MNC, NC-MNC, and MNEC nanostructures are ideal for producing pronounced tunable Fano resonances and higher order dark hybridized modes in the visible and near infrared region, which may be useful for plasmon sensing, electromagnetic-induced transparency, lasing, slowing light, switching, and SERS applications.

References

1. Kelly KL, Coronado E, Zhao LL, Schatz GC (2003) The optical properties of metal nanoparticles: the influence of size, shape, and dielectric environment. The Journal of Physical Chemistry B 107(3):668–677

2. Banaee MG, Crozier KB (2010) Mixed dimer double-resonance substrates for surface-enhanced Raman spectroscopy. Acs Nano 5(1):307–314

3. Liu C, Mi C, Li B (2011) The plasmon resonances of multilayered gold nanoshells and their potential bio-applications. Nanotechnology IEEE Transactions on 10(99):797–805

4. Sheikholeslami S, Garcia-Etxarri A, Dionne JA (2011) Controlling the interplay of electric and magnetic modes via Fano-like plasmon resonances. Nano letters 11(9):2694–2701

5. Knight MW, Halas NJ (2008) Nanoshells to nanoeggs to nanocups: optical properties of reduced symmetry core–shell nanoparticles beyond the quasistatic limit. New Journal of Physics 10:105006

6. Mirin NA, Ali TA, Nordlander P, Halas NJ (2010) Perforated semishells: far-field directional control and optical frequency magnetic response. Acs Nano 4(5):2701–2712

7. Yang ZJ, Zhang ZS, Zhang LH, Li QQ, Hao ZH, Wang QQ (2011) Fano resonances in dipole-quadrupole plasmon coupling nanorod dimers. Opt Lett 36(9):1542–1544

8. Hao F, Nordlander P, Sonnefraud Y, Dorpe PV, Maier SA (2009) Tunability of subradiant dipolar and Fano-type plasmon resonances in metallic ring/disk cavities: implications for nanoscale optical sensing. Acs Nano 3(3):643–652

9. Aizpurua J, Hanarp P, Sutherland D, Käll M, Bryant GW, Garcia de Abajo F (2003) Optical properties of gold nanorings. Phys Rev Lett 90(5):57401

10. Grand J, Adam PM, Grimault AS, Vial A, Lamy De La Chapelle M, Bijeon JL, Kostcheev S, Royer P (2006) Optical extinction spectroscopy of oblate, prolate and ellipsoid shaped gold nanoparticles: experiments and theory. Plasmonics 1(2):135–140

11. Khoury CG, Norton SJ, Vo-Dinh T (2009) Plasmonics of 3-D nanoshell dimers using multipole expansion and finite element method. Acs Nano 3(9):2776–2788

12. Fan JA, Bao K, Wu C, Bao J, Bardhan R, Halas NJ, Manoharan VN, Shvets G, Nordlander P, Capasso F (2010) Fano-like interference in self-assembled plasmonic quadrumer clusters. Nano letters 10(11):4680–4685

13. Luk'yanchuk B, Zheludev NI, Maier SA, Halas NJ, Nordlander P, Giessen H, Chong CT (2010) The Fano resonance in plasmonic nanostructures and metamaterials. Nat Mater 9(9):707–715

14. Rahmani M, Lukiyanchuk B, Ng B, Liew Y, Hong M (2011) Generation of pronounced Fano resonances and tuning of subwavelength spatial light distribution in plasmonic pentamers. Opt Express 19(6):4949–4956

15. Wang M, Cao M, Chen X, Gu N (2011) Subradiant plasmon modes in multilayer metal-dielectric nanoshells. J Phys Chem C 115(43):20920–20925

16. Prodan E, Radloff C, Halas N, Nordlander P (2003) A hybridization model for the plasmon response of complex nanostructures. Science 302(5644):419–422

17. Chen J, Wang P, Chen C, Lu Y, Ming H, Zhan Q (2011) Plasmonic EIT-like switching in bright-dark-bright plasmon resonators. Opt Express 19(7):5970–5978

18. Mukherjee S, Sobhani H, Lassiter JB, Bardhan R, Nordlander P, Halas NJ (2010) Fanoshells: nanoparticles with built-in Fano resonances. Nano letters 10(7):2694–2701

19. Zhang S, Bao K, Halas NJ, Xu H, Nordlander P (2011) Substrate-induced Fano resonances of a plasmonic nanocube: a route to increased-sensitivity localized surface plasmon resonance sensors revealed. Nano letters 11(4):1657–1663

20. Fang Z, Cai J, Yan Z, Nordlander P, Halas NJ, Zhu X (2011) Removing a wedge from a metallic nanodisk reveals a Fano resonance. Nano letters 11(10):2694–2701

21. Mirin NA, Bao K, Nordlander P (2009) Fano resonances in plasmonic nanoparticle aggregates†. J Phys Chem A 113(16):4028–4034

22. Bardhan R, Mukherjee S, Mirin NA, Levit SD, Nordlander P, Halas NJ (2009) Nanosphere-in-a-nanoshell: a simple nanomatryushka†. J Phys Chem C 114(16):7378–7383

23. Johnson PB, Christy R (1972) Optical constants of the noble metals. Physical Review B 6(12):4370–4379

24. Qian J, Wang W, Li Y, Xu J, Sun Q (2012) Optical extinction properties of perforated gold-silica-gold multilayer nanoshells. J Phys Chem C 116(18):10349–10355

25. Hu Y, Fleming RC, Drezek RA (2008) Optical properties of gold-silica-gold multilayer nanoshells. Opt Express 16(24):19579–19591

26. Hu Y, Noelck SJ, Drezek RA (2010) Symmetry breaking in gold–silica–gold multilayer nanoshells. Acs Nano 4(3):1521–1528

27. Wu DJ, Jiang SM, Liu XJ (2011) Tunable Fano resonances in three-layered bimetallic Au and Ag nanoshell. J Phys Chem C 115(48):23797–23801

28. Ho JF, Luk'yanchuk B, Zhang JB (2012) Tunable Fano resonances in silver–silica–silver multilayer nanoshells. Applied Physics A: Materials Science & Processing 107(1):133–137

29. Jian Z, Jian-jun L, Jun-wu Z (2011) Tuning the dipolar plasmon hybridization of multishell metal-dielectric nanostructure: gold nanosphere in a gold nanoshell. Plasmonics 6(3):527–534

30. Hao F, Sonnefraud Y, Dorpe PV, Maier SA, Halas NJ, Nordlander P (2008) Symmetry breaking in plasmonic nanocavities: subradiant LSPR sensing and a tunable Fano resonance. Nano letters 8(11):3983–3988

31. Gallinet B, Martin OJF (2011) Relation between near-field and far-field properties of plasmonic Fano resonances. Opt Express 19(22):22167–22175